Geophysical Research Letters

Supporting Information for

Revealing crustal deformation and strain rate in Taiwan using InSAR and GNSS

Kathryn R. Franklin and Mong-Han Huang

Department of Geology, University of Maryland, College Park, MD, USA

Contents of this file

Texts S1 to S3
Figures S1 to S13

Additional Supporting Information

Dataset S1: 3-D interseismic velocities
Dataset S2: Strain rate products

Introduction

Text S1 describes InSAR time series processing.
Text S2 describes GNSS and InSAR uncertainty assessment.
Text S3 describes the estimation of surface strain rate.
Figure S1 shows examples of GNSS and InSAR time series fittings.
Figure S2 shows RMS misfits of GNSS and InSAR.
Figure S3 shows uncertainty of InSAR-GNSS combined 3-D velocities.
Figure S4 shows RMS misfits for determining the τ value.
Figure S5 shows the variance with pixel distance in a semi-variogram.
Figure S6 shows the downsampled semi-variogram that highlights the characteristic distance.
Figure S7 shows strain rate maps with different level of smoothing.
Figure S8 shows a schematic of maximum and minimum principal strains.
Figure S9 shows an overview of principal strain rates of Taiwan.
Figure S10 shows an overview of principal strain rates of Taiwan.
Figure S11 shows an overview of dilatation rates of Taiwan.
Figure S12 shows an overview of second invariant of the strain rate tensors of Taiwan.
Figure S13 shows an overview of rotation rates of Taiwan.

Supplementary Text S1: Time Series Processing

For a more in-depth data analysis, a module developed by *Huang and Evans* (2019) was used to (i) re-model the time-series for the ascending and descending LOS InSAR velocities using a polynomial and (ii) re-estimate the ascending and descending LOS InSAR mean velocities to include a GNSS correction.

To exclude low-quality pixels from the ascending track and descending track LOS InSAR data, the temporal and spatial coherence thresholds of the mean ascending and descending LOS InSAR velocities were determined through a trial-and-error method of pixel visibility. Temporal coherence refers to the stability of a pixel throughout time – how similar the pixel phase is between acquisitions. The more stable a pixel, the higher the temporal coherence. Deformation reduces the temporal coherence within reason. Spatial coherence refers to the consistency of a pixel's phase to surrounding pixels. Sharp phase changes between neighboring pixels may indicate an error. We used a temporal coherence threshold of 0.3 for west and east Taiwan, and a spatial coherence threshold of 0.4 for west Taiwan and east Taiwan. The average of the temporal and spatial coherence values above the defined thresholds was determined to be the final coherence value. This final value must be above the final predefined mask value of 0.35. Applying this mask excluded all pixels with values lower than the final coherence value.

After the ascending and descending LOS InSAR velocities were masked, (i) the elevation of each pixel for each interferogram was defined using the DEM, (ii) the look angles and heading directions for each interferogram were defined, (iii) the reference image was set to the first acquisition date for both the ascending and descending track interferograms, and (iv) the latitude and longitude data for the bounding box were linked to the module to geolocate each pixel in each interferogram.

The west Taiwan ascending and descending LOS InSAR velocities were assigned a local reference region in the west, and the east Taiwan ascending and descending LOS InSAR velocities were assigned a local reference region in the east. The designated reference regions were at an area without known faults and minimal seasonal surface movement due to hydrologic cycles and human induced land subsidence. Subsequently, the reference regions were considered as stable regions with zero movement. Once the reference region was defined, the mean velocity of each pixel location throughout time was determined.

To fit the time-series of each pixel for ascending and descending LOS InSAR velocities for both west and east Taiwan, we generated a mathematical model with a linear velocity term, annual periodic terms, and semi-annual periodic terms (Equation S1). The terms utilized match the general pattern of interseismic deformation anticipated in Taiwan. For example, the linear

velocity term accounted for the overall mean velocity of the pixel, the annual periodic terms took into consideration the wet and dry seasons' influence on motion, and the semi-annual periodic terms considered sub-tropical precipitation events (e.g., monsoon vs. typhoon events). These terms for a pixel at location (*x,y*) were represented as:

$$LOS(x,y,t_i) = m_1(x,y) + m_2(x,y)t_i + m_3(x,y)\sin(2\pi t_i) + m_4(x,y)\cos(2\pi t_i) + m_5(x,y)\sin(4\pi t_i) + m_6(x,y)\cos(4\pi t_i) + m_7(x,y)H(t_{\mathrm{EQ}}) + m_8(x,y)\,H(t_{\mathrm{EQ}})\ln\left[1+\left(\frac{t_i - t_{\mathrm{EQ}}}{\tau}\right)\right] \quad \text{[S1]}$$

where m_1 is a constant representing a constant adjustment for the time-series, m_2 is the linear trend of the pixel throughout time, m_3 and m_4 are the annual seasonality of the pixel throughout time, m_5 and m_6 are the semiannual seasonality of the pixel throughout time, m_7 is the Hualien earthquake (i.e., a notable earthquake within the timeframe of interest) displacement coefficient, $H(t_{\mathrm{EQ}})$ is the step function to remove the 2018 M_W 6.4 Hualien Earthquake coseismic event, m_8 represents the postseismic period with a relaxation time of τ = 121 days (See **Text S2.1** for determining this value).

Now, assuming ***G*** matrix represents the mathematical model described in Equation S1,

$$\vec{d} = \boldsymbol{G}\vec{m} \quad \text{[S2]}$$

where $\vec{d}$ is the data vector (LOS (*x, y, t*)), ***G*** is the mathematical model that relates the model parameters to the data (right hand side of Equation S1), and $\vec{m}$ is the model vector (m_1, m_2, m_3, m_4, m_5, m_6, m_7, m_8). This mathematical model enables the fitting of a time-series at each pixel location throughout time for both the ascending and descending track data for both west and east Taiwan.

We used a least squares inversion to solve for the mathematical model and estimate the coefficient of each term. This solving approach minimizes the sum of squares of the residuals (Equation S3).

$$\vec{m} = (\boldsymbol{G}^{\boldsymbol{T}}\boldsymbol{G})^{-1}\boldsymbol{G}^{\boldsymbol{T}}\vec{d} \quad \text{[S3]}$$

where $\vec{m}$ is the model vector, ***G*** is the mathematical model, $\boldsymbol{G}^{\boldsymbol{T}}$ is the transpose of the mathematical model, and $\vec{d}$ is the data vector.

Then, using the pre-processed time-series of each GNSS station, we applied a GNSS-correction to the mean velocities of each pixel derived from the calculated time-series. This correction applied the accuracy of GNSS to the high spatial resolution of InSAR. The GNSS-correction only considered the same time period as the InSAR data and was comparable to the LOS InSAR data as the displacements were projected onto the satellite look angle and heading direction.

To apply the GNSS correction to the ascending and descending LOS InSAR velocities, a ramp model that best fit the InSAR and GNSS data velocity differences was constructed. The coefficients of the ramp model were solved for by inversion (Equation S3) with the velocity residuals as data. Removing the ramp from the uncorrected ascending and descending LOS InSAR velocities produced the GNSS-corrected ascending and descending LOS InSAR velocities. Additionally, the ascending and descending ramps for west and east Taiwan could be applied to the time-series for GNSS correction inclusion.

S1.1 Merge Ascending and Descending from East and West Taiwan

To begin merging the ascending and descending LOS InSAR velocities from west and east Taiwan, the low coherence (or low quality) pixels (e.g., pixels capturing water) from each dataset were masked out and set to 0. High coherence pixels were set to 1, and pixels that were high coherence in both datasets were set to 2. During the GNSS correction, west and east Taiwan were assigned the same reference location; therefore, here, they were merged without searching for a common reference region. For accuracy purposes, if there were overlapping real valued pixels from both datasets, the pixels from the east Taiwan dataset were kept while the pixels from the west Taiwan dataset were set to 0. This merged masking process was done for both the ascending and descending LOS InSAR velocities. Once the masks were created, the values of the real-valued pixels were utilized and datasets with ascending LOS InSAR velocities and descending LOS InSAR velocities for all of Taiwan were created.

S1.2 Convert GNSS-Corrected LOS InSAR & GNSS Velocities

GNSS-corrected LOS InSAR velocities and GNSS velocities were utilized to estimate 3-D deformation: east-west, north-south, and vertical components. First, the GNSS velocities were interpolated to InSAR pixels using 2-D cubic interpolation in Matlab. The mesh size matched the pixel location and size of that from InSAR geocoded to the DEM. The inclusion of these velocities

enabled a more accurate 3-D velocity field of Taiwan to be constructed as, for example, InSAR has poor sensitivity to north-south velocities and GNSS velocities are less sensitive to atmospheric phase delays.

The GNSS-corrected LOS InSAR velocities and interpolated GNSS velocities were converted to 3-D deformation by relating the heading direction and look angle of the satellites to the velocity data through an inverse problem in the form of Equation S2. The final velocity product was as follows (Equation S4):

$$\begin{bmatrix} LOS_A \\ LOS_D \\ GNSS_E \\ GNSS_N \\ GNSS_Z \end{bmatrix} = \begin{bmatrix} \cos\phi_A \sin\theta_A & \sin\phi_A \sin\theta_A & -\cos\theta_A \\ \cos\phi_D \sin\theta_D & \sin\phi_D \sin\theta_D & -\cos\theta_D \\ 1 & 0 & 0 \\ 0 & 1 & 0 \\ 0 & 0 & 1 \end{bmatrix} \begin{bmatrix} U_E \\ U_N \\ U_Z \end{bmatrix} \quad [S4]$$

where data vector $\vec{d}$ contains: $LOS_{A,D}$ the LOS velocity for the ascending and descending tracks and $GNSS_{E,N,Z}$ the interpolated GNSS velocities in east, north, and vertical, respectively. Matrix $\boldsymbol{G}$ contains: ϕ_A and ϕ_D the satellite heading direction for the ascending and descending tracks and θ_A and θ_D the satellite look-angle of the ascending and descending tracks, respectively. This matrix relates the InSAR and GNSS velocities to their 3-D components. Model vector $\vec{m}$ contains the 3-D velocity outputs $U_{E,N,Z}$.

The linear inverse problem was solved for using a least squares inversion to minimize the sum of squares of residuals and to determine the best fit model (Equation S3). Additionally, in order to weigh each component of the output 3-D velocity dataset based on misfit, we incorporated a weighting matrix $\boldsymbol{W}$ into the least squares inversion (Equation S5).

$$\vec{m} = (\boldsymbol{G^T W G})^{-1} \boldsymbol{G^T W^T} \vec{d} \quad [S5]$$

where matrix $\boldsymbol{W}$ (Equation S6) is used to weigh the data and is solved for during **Text S2.1**.

$$\boldsymbol{W} = \begin{bmatrix} {\varepsilon_A}^{-2} & 0 & 0 & 0 & 0 \\ 0 & {\varepsilon_D}^{-2} & 0 & 0 & 0 \\ 0 & 0 & {\varepsilon_{GNSS_E}}^{-2} & 0 & 0 \\ 0 & 0 & 0 & {\varepsilon_{GNSS_N}}^{-2} & 0 \\ 0 & 0 & 0 & 0 & {\varepsilon_{GNSS_Z}}^{-2} \end{bmatrix} \quad [S6]$$

where matrix $\boldsymbol{W}$ is the weighting matrix and ε for ascending, descending, and GNSS represents the misfit values produced from the inversion of Equation S1.

Using the resulting 3-D velocity outputs, the Final InSAR and GNSS (FIG) dataset was created. This dataset includes: the weighted mean GNSS-corrected InSAR / interpolated GNSS velocity values with the associated uncertainties and the GNSS velocity values with the associated uncertainties. The GNSS velocity values were appended to the dataset for additional data point inclusion. Uncertainties are solved during **Text S2.2**. Additionally, a Reduced FIG dataset was created, which contained the values within the FIG dataset downsampled to every 10 pixels in both the x- and y-direction. The FIG and Reduced FIG datasets contain pixels that are 50 m x 50 m and 500 m x 500 m, respectively.

Supplementary Text S2: Error Analysis

We incorporated an error analysis into the InSAR and GNSS velocity solutions by determining root mean square (RMS) misfit. As previously mentioned, the calculated misfit was used to define the weighting matrix, ***W*** (Equation S6), to properly weigh between the GNSS-corrected InSAR and the interpolated GNSS velocities. The uncertainties, inferred from misfit, produced by taking the LOS and GNSS velocities to east-west, north-south, and vertical were utilized to confirm consistent transformation and were appended to the FIG dataset for later usage. Furthermore, to distinguish tectonic signal from noise in the deformation rate analysis, we quantified distance-correlated noise structure using a semi-variogram and covariogram model for a region without known surface deformation.

S2.1 Solving for RMS Misfit and τ

When constructing the mathematical model (Equation S1) that best fits the velocity data, we calculated the RMS misfit to detail the misfit between the model and the observed velocity values (Equation S8). Specifically, the RMS misfit was calculated for the ascending and descending LOS InSAR data (every pixel in every scene) and the east-west, north-south, and vertical GNSS data (every station in every epoch). Since west and east Taiwan were processed separately, the west and east Taiwan InSAR misfits were calculated separately and then merged.

$$E(x,y) = \sqrt{\frac{1}{N}\sum_{i=1}^{N}\left(\vec{d}_i(x,y) - \vec{m}_i(x,y)\right)^2} \quad for\ i = 1, \dots N; \qquad [S8]$$

where $E(x,y)$ is the RMS misfit of pixel (x,y), $\vec{d}_i$ is observed velocity data, and $\vec{m}_i$ is best fit model velocity data, i is the index of an acquisition, and N is the total number of acquisitions.

Additionally, to determine the relaxation time (τ) for removing the postseismic contribution from the 2018 M_W *6.4* Hualien Earthquake in the mathematical model (Equation S1), we calculated the RMS misfit of all the pixels with a given τ value between 1 and 600 days in a 20-day step size:

$$E(\tau_j) = \sqrt{\frac{1}{N}\sum_{i=1}^{N}(\vec{d}_i(\tau_j) - \vec{m}_i(\tau_j))^2} \quad for\ i = 1, \dots N;\ j = 1, \dots 600\ (\text{days}); \qquad [S9]$$

where $E(\tau_j)$is the RMS misfit of relaxation time (τ) in j days, $\vec{d}_i$ is observed velocity data, and $\vec{m}_i$ is best fit model velocity data, i is the index of an acquisition, and N is the total number of

acquisitions. The relaxation time that produced the least amount of misfit was used in Equation S1.

S2.2 Uncertainty Assessment

The uncertainty of every pixel was solved by evaluating the misfit of the inversion that transformed the LOS InSAR and GNSS velocities to 3-D velocities. The uncertainty values at each time were inferred from the velocity misfit values using a linear inverse problem in the $\vec{d} = \boldsymbol{G}\vec{m}$ form (Equation S10):

$$\begin{bmatrix} \varepsilon_A(x,y) \\ \varepsilon_D(x,y) \\ \varepsilon\ GNSS_E(x,y) \\ \varepsilon\ GNSS_N(x,y) \\ \varepsilon\ GNSS_Z(x,y) \end{bmatrix} = \begin{bmatrix} \cos\phi_A(x,y)\sin\theta_A(x,y) & \sin\phi_A(x,y)\sin\theta_A(x,y) & -\cos\theta_A(x,y) \\ \cos\phi_D(x,y)\sin\theta_D(x,y) & \sin\phi_D(x,y)\sin\theta_D(x,y) & -\cos\theta_D(x,y) \\ 1 & 0 & 0 \\ 0 & 1 & 0 \\ 0 & 0 & 1 \end{bmatrix} \begin{bmatrix} Unc_E(x,y) \\ Unc_N(x,y) \\ Unc_Z(x,y) \end{bmatrix} \quad [S10]$$

where data vector $\vec{d}$ contains: $\varepsilon_{A,D}(x,y)$ the misfit for the ascending and descending track pixels and $\varepsilon\ GNSS_{E,N,Z}(x,y)$ the interpolated GNSS misfit for east, north, and vertical, respectively. Matrix $\boldsymbol{G}$ contains: ϕ_A and ϕ_D the satellite heading direction for the ascending and descending tracks and θ_A and θ_D the satellite look-angle of the ascending and descending tracks, respectively. This matrix relates the GNSS-corrected InSAR / interpolated GNSS velocities to their 3-D components. Model vector $\vec{m}$ contains the 3-D velocity uncertainty estimates, $Unc_{E,N,Z}$, for east, north, and vertical components, respectively. The identity matrix is used to bring the GNSS misfit values through the inverse problem with no transformation as they are already in 3-D form.

S2.3 Noise Structure Contributions in the Deformation Rate Analysis

To determine which level of smoothing best eliminated the noise structure contribution, I calculated a semi-variogram model and covariogram model of a non-deforming region for error estimation (*Sudhaus and Jonsson*, 2009). The semi-variogram was modeled from pixel variance with distance in the x- and y-direction (Equation S11) and suggested the use of an exponential equation to model the covariogram (Equation S12). The covariogram estimated pixel spatial correlation with distance (i.e., covariance) (*Sudhaus and Jonsson*, 2009).

The semi-variogram was defined as (Equation S11):

$$S(r) = \sigma^2(1 - e^{-\frac{r}{\lambda}}) \quad [S11]$$

where $S(r)$ is the modeled semi-variogram between two pixels, σ^2 is the variance, r is the distance between the two pixels, and λ is the characteristic wavelength of the transect.

The modeled covariogram, produced from an exponential mathematical model, was defined as (Equation S12):

$$C(r) = \sigma^2 e^{-\frac{r}{\lambda}} \quad \text{[S12]}$$

where $C(r)$ is the covariance between two pixels, σ^2 is the variance, r is the distance between the two pixels, and λ is the characteristic wavelength of the transect.

The modeled semi-variogram was solved for with an exponential, spherical, and gaussian mathematical model. The exponential model fit best and was subsequently utilized to model the covariogram. The unknown σ^2 and λ in the covariogram model (Equation S12) were solved using an inverse problem with the FIG dataset velocities for a non-deforming region as data constraints. The covariogram model acted to estimate the characteristic wavelength of correlation to quantify the assumption that variables closer in distance tend to be more similar (Watson et al., 2022; Hussain et al., 2016). Therefore, a smoothing window size that is smaller than the characteristic distance λ at which pixels were spatially correlated may display noise signals and not accurately capture the tectonic deformation influencing the region. Given that the deformation tensor was calculated every 1 km and each pixel is 500 m x 500 m in the Reduced FIG dataset, utilizing the nearest 30, 144, and 420 pixels resulted in a 1.5, 3.4, and 5.8 km radius of values being incorporated into the tensor, respectively (**Figure S7**).

Supplementary Text S3: Deformation rate analysis

S3.1 Dilatation, Maximum Shear, and 2nd Invariant

The deformation tensor defines position change within a body due to external forces (**Figure S8**). Using the Reduced FIG dataset, I determined the deformation rate tensor every 1 km where the InSAR samples were located every 500 m. The calculated deformation rate tensors considered the nearest 30, 144, and 420 pixels. From this, we calculated dilatation (unit: yr^{-1}), maximum shear (unit: yr^{-1}), and 2nd invariant (unit: yr^{-1}). Note: Dilatation, maximum shear, and 2nd invariant refer to their rate per year. The purpose of the deformation rate analysis was to quantify 2-D deformation fields across Taiwan. This analysis assumed that deformation fields were subject to variations in stress rather than strength (Fagereng and Biggs, 2019).

The deformation rate tensor is defined as:

$$\dot{\boldsymbol{D}} = \begin{bmatrix} \dot{D}_{xx} & \dot{D}_{xy} \\ \dot{D}_{yx} & \dot{D}_{yy} \end{bmatrix}$$

$$= \begin{bmatrix} \dot{D}_{xx} & \frac{1}{2}\left(\dot{D}_{xy} + \dot{D}_{yx}\right) \\ \frac{1}{2}\left(\dot{D}_{xy} + \dot{D}_{yx}\right) & \dot{D}_{yy} \end{bmatrix} + \begin{bmatrix} 0 & \frac{1}{2}\left(\dot{D}_{xy} - \dot{D}_{yx}\right) \\ -\frac{1}{2}\left(\dot{D}_{xy} - \dot{D}_{yx}\right) & 0 \end{bmatrix}$$

$$= \begin{bmatrix} \frac{\partial V_E}{\partial x} & \frac{1}{2}\left(\frac{\partial V_E}{\partial y} + \frac{\partial V_N}{\partial x}\right) \\ \frac{1}{2}\left(\frac{\partial V_E}{\partial y} + \frac{\partial V_N}{\partial x}\right) & \frac{\partial V_N}{\partial y} \end{bmatrix} + \begin{bmatrix} 0 & \frac{1}{2}\left(\frac{\partial V_E}{\partial y} - \frac{\partial V_N}{\partial x}\right) \\ -\frac{1}{2}\left(\frac{\partial V_E}{\partial y} - \frac{\partial V_N}{\partial x}\right) & 0 \end{bmatrix} \quad \text{[S13]}$$

where the deformation rate tensor, $\dot{\boldsymbol{D}}$, is the sum of the strain rate (irrotational) matrix and rotational rate matrix. $\frac{\partial V_E}{\partial x} = \dot{D}_{xx}$, $\frac{\partial V_N}{\partial y} = \dot{D}_{yy}$, and $\frac{1}{2}\left(\frac{\partial V_E}{\partial y} + \frac{\partial V_N}{\partial x}\right) = \frac{1}{2}\left(\dot{D}_{xy} + \dot{D}_{yx}\right)$. The off-diagonal terms in the rotational matrix are equal in quantity but change in sign.

Using components of the deformation rate tensor, I solved for dilatation, the overall change in volume due to deformation. Dilatation is the sum of principal strains, which are the eigenvalues of a strain rate tensor (Equations S14 & S15).

$$| \mathbf{A} - \lambda \cdot \mathbf{I} | = 0 \quad \text{[S14]}$$

where **A** is the strain tensor, λ are the eigenvalues, and **I** is the identity matrix. The | | sign represents the determinant operation.

$$\delta = \varepsilon_1 + \varepsilon_2 \quad \text{[S16]}$$

where δ is dilatation and ε_1 and ε_2 are the maximum and minimum principal strains (i.e., eigenvalues).

Then, maximum shear was solved to determine the factor in which deformation occurred in a specific direction (Equation S16). In this case, maximum shear (i.e., change in shape/angle) corresponds to the greatest shear at 45° to the principal strains.

$$\gamma_{max} = \frac{\varepsilon_1 - \varepsilon_2}{2} \quad \text{[S16]}$$

where γ_{max} is maximum shear and ε_1 and ε_2 represent the maximum and minimum principal strains (i.e., eigenvalues).

Invariants of the deformation rate tensor are properties that do not change under coordinate rotation. The 2nd invariant of strain rate determines the total strain rate accumulation of the area of interest, which highlights localities with increased seismic risk (Equation S17) (Pagani et al., 2021). It acts as a combination of both the dilatation (contraction and extension) and maximum shear stress.

$$I_2 = \sqrt{D_{xx}^2 + D_{yy}^2 + 2\left[\frac{1}{2}(D_{xy} + D_{yx})\right]^2} \quad \text{[S17]}$$

where I_2 is 2nd invariant of strain rate and D_{xx}, D_{yy}, D_{xy}, D_{yx} are components of the symmetric strain rate tensor. D_{xy} and D_{yx} cannot be assumed to be of the same value as rotation, which does not address shape change and is not taken into consideration.

Supplementary Figures

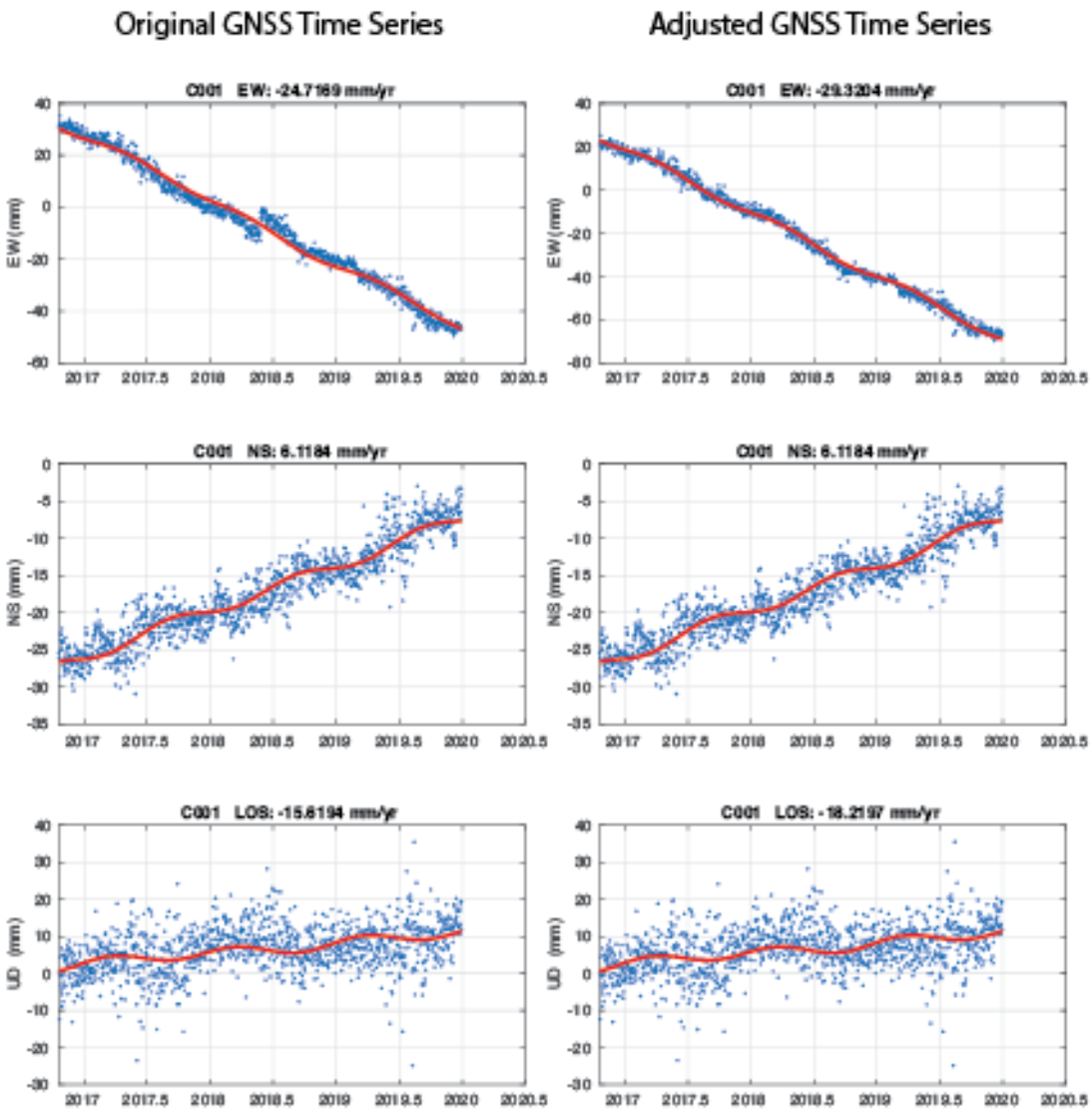

Figure S1. Example of GNSS time-series manual adjustment showing the original time-series of GNSS station C001 in Taiwan (lat/lon: 23.418/120.612) and the adjusted time-series of GNSS station C001. The adjustment is located at 2018.4 in the east-west motion time-series.

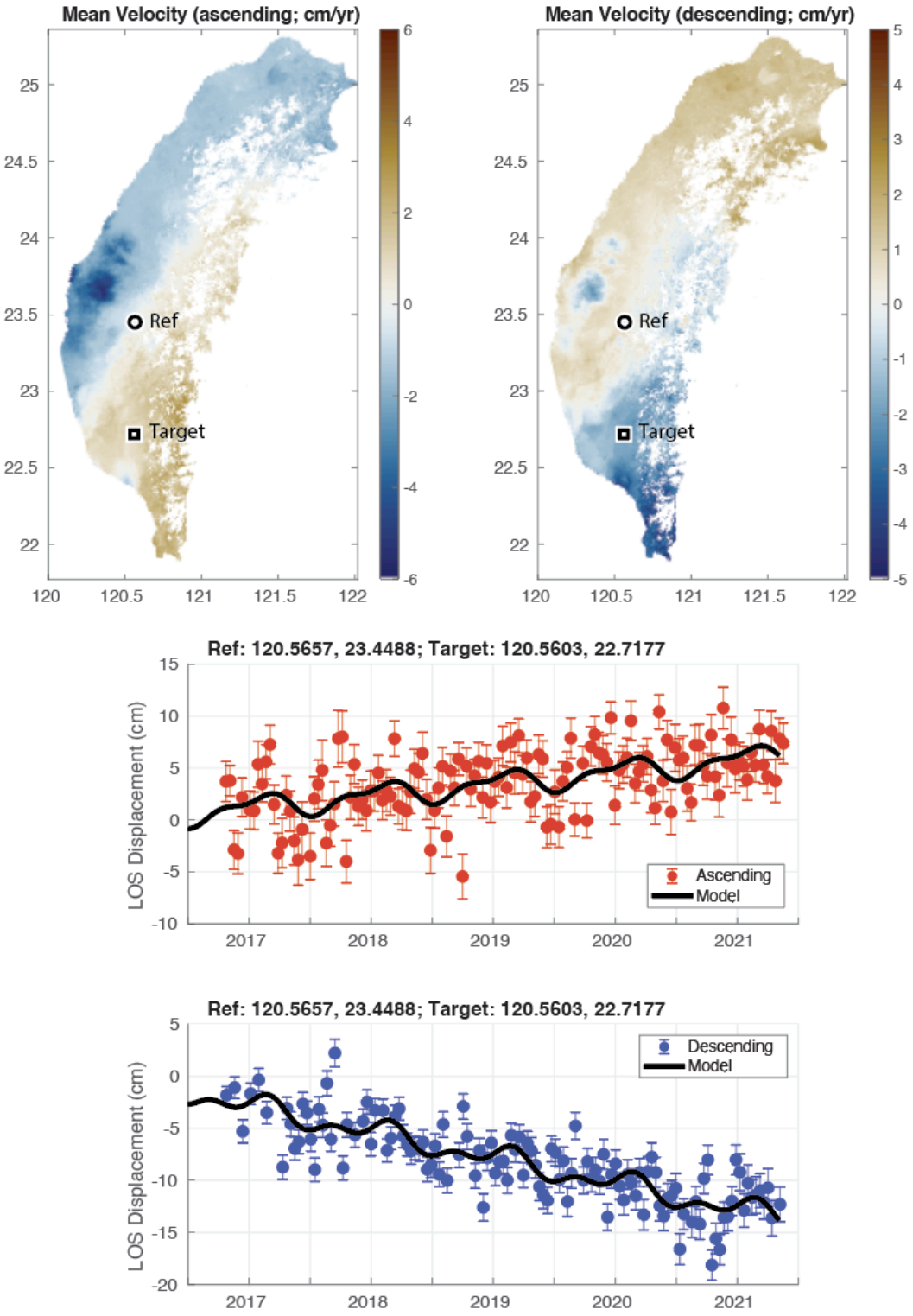

Figure S1 (cont.). Example InSAR time series for west Taiwan. The two maps show mean velocity in ascending and descending tracks. The time series are motions relative to the reference point (lat/lon shown in the title of the time series plot). The back curve is the modeled time series using Equation S1.

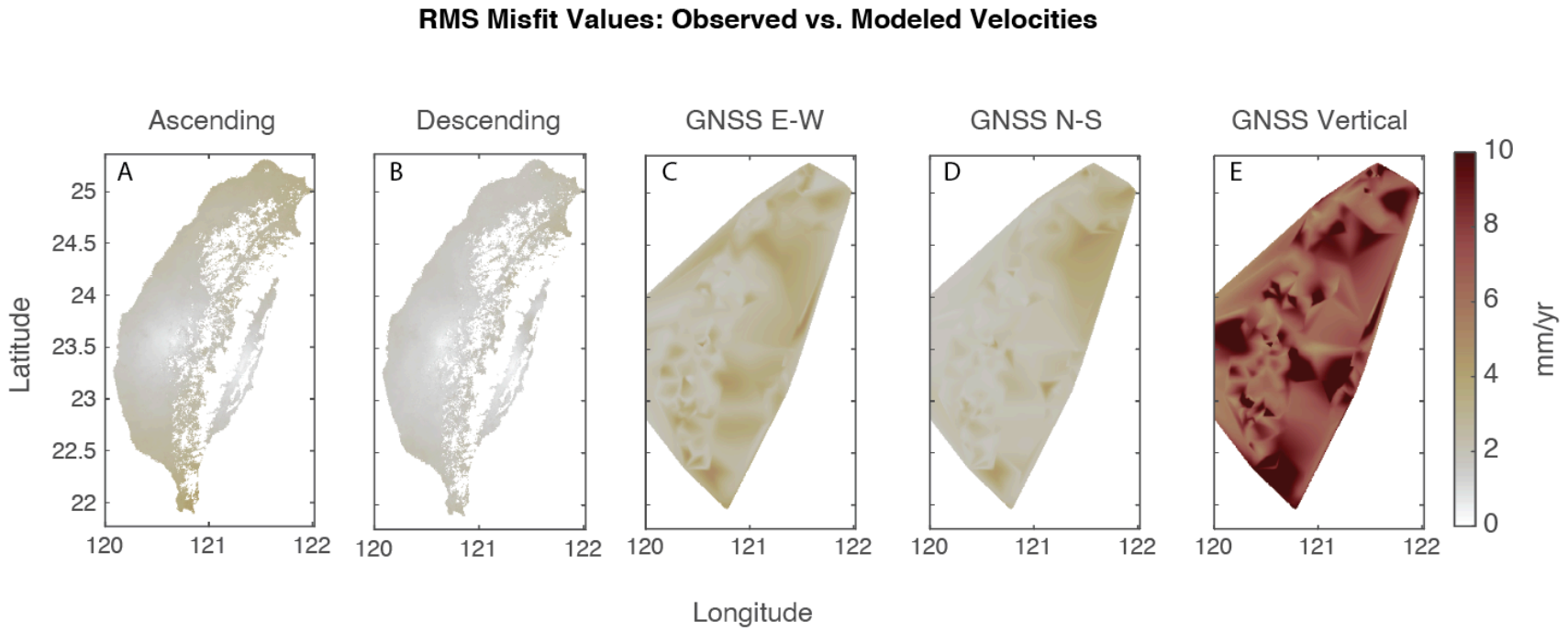

Figure S2. RMS misfits produced from the transformation of observed (A) ascending and (B) descending LOS InSAR velocities and interpolated (C) east-west, (D) north-south, and (E) vertical GNSS velocities to modeled velocity values.

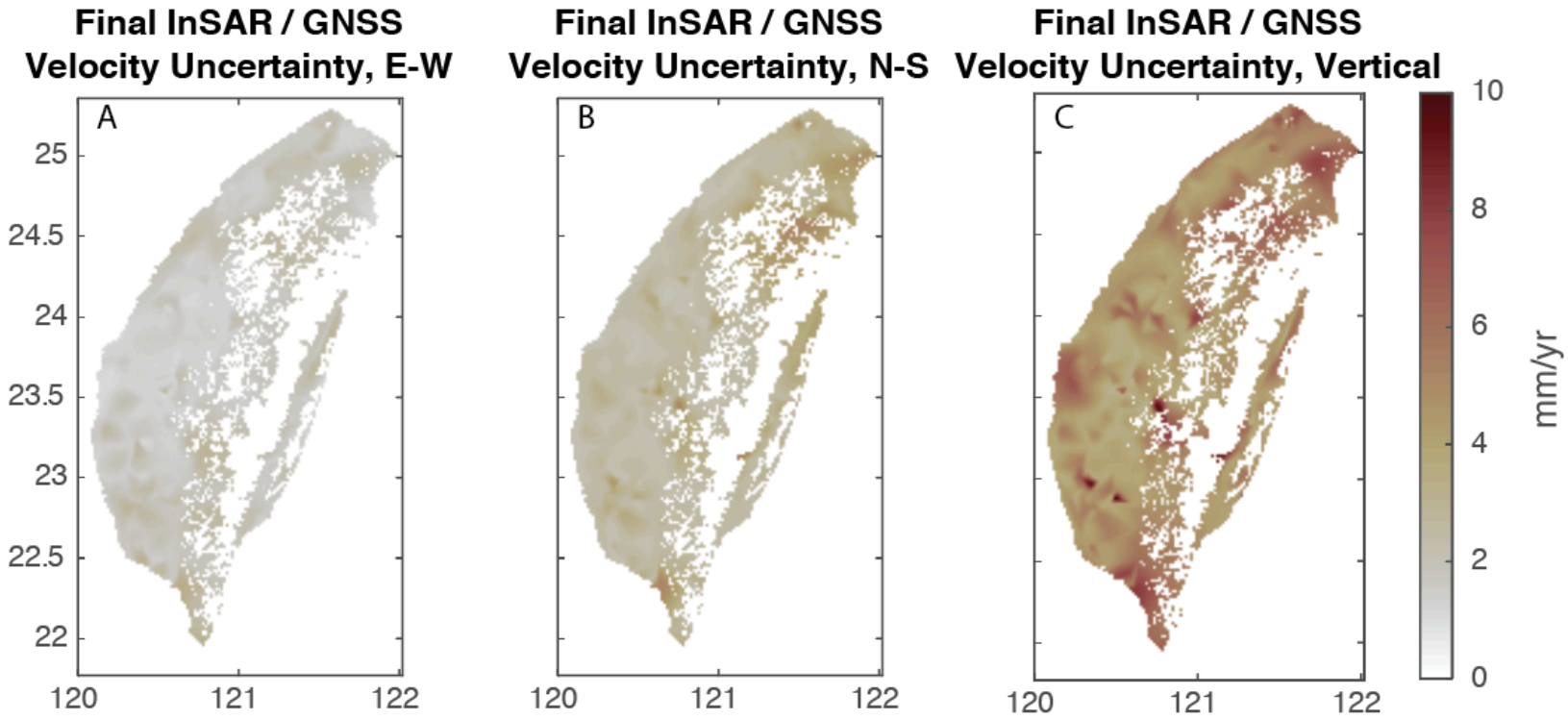

Figure S3. Uncertainty values produced from transforming GNSS-corrected ascending and descending LOS InSAR velocities and interpolated GNSS velocities to the FIG dataset with (A) east-west, (B) north-south, and (C) vertical velocities.

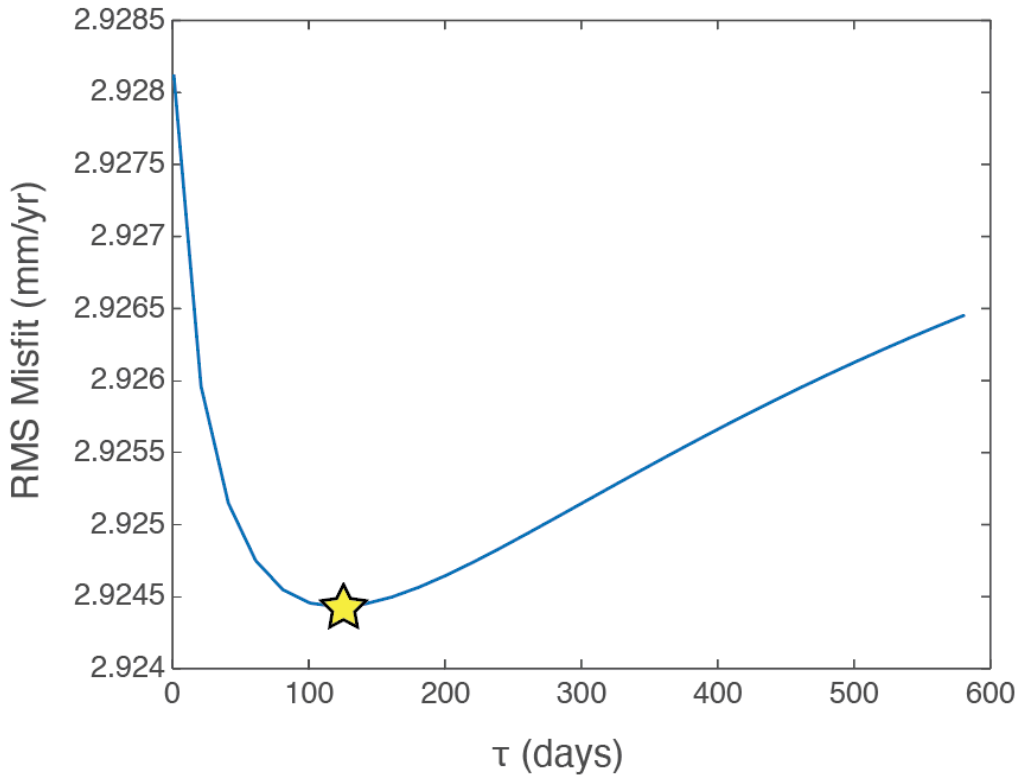

Figure S4. RMS misfits produced from utilizing various τ values (0 to 600 days in 20-day step sizes) in the transformation of observed velocities to modeled velocities. The yellow star indicates τ = 121, which is associated with the lowest RMS misfit estimation.

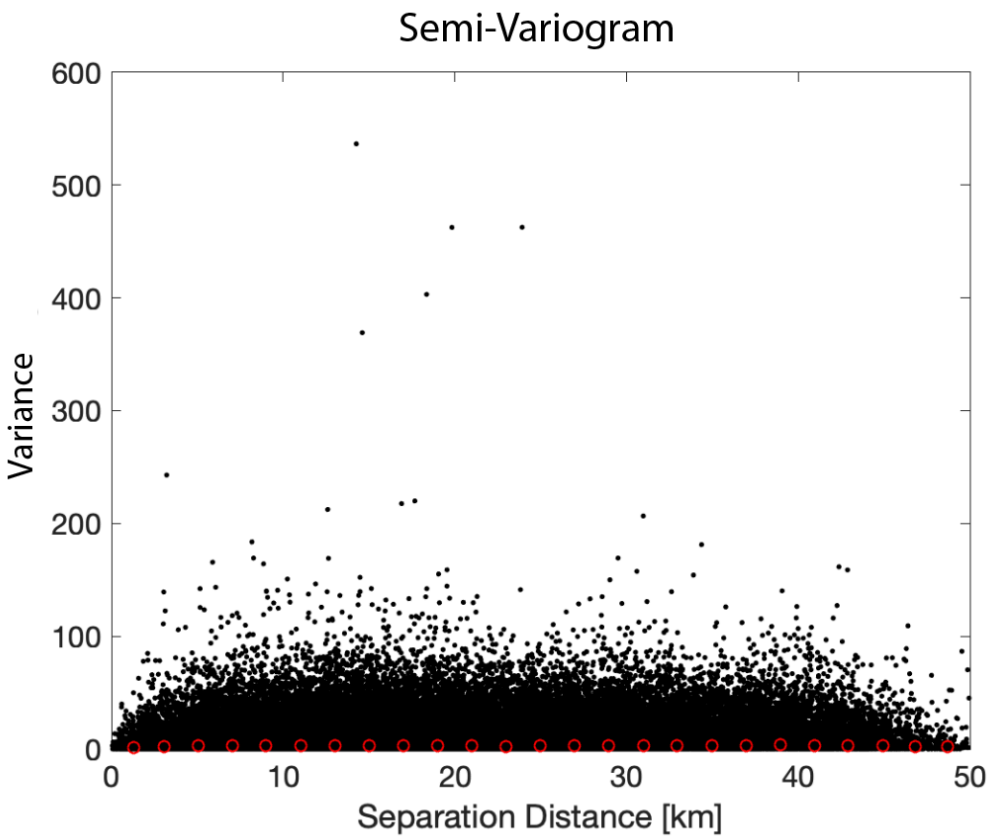

Figure S5. Semi-variogram displaying variance as a function of separation distance for each and all pixels. The open red circles represent the relative locations along the x-axis used for binning the data.

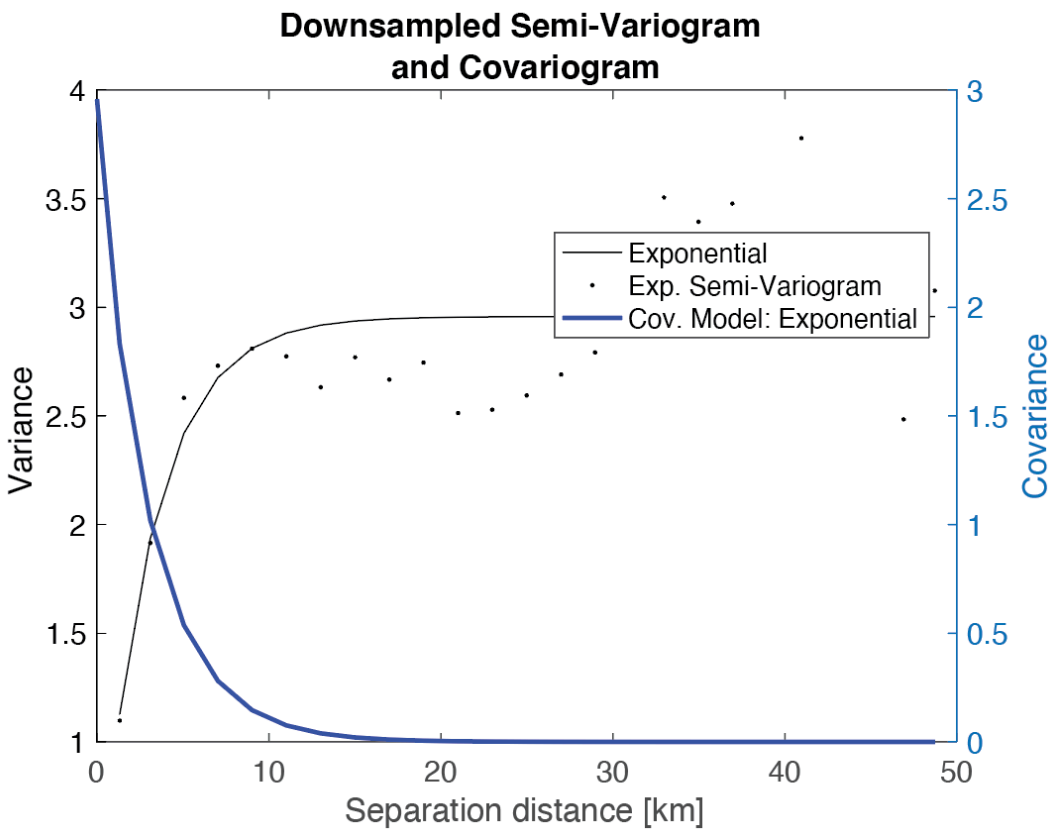

Figure S6. Downsampled semi-variogram displaying variance between each and all pixels as a function of distance. Overlain is the best fit exponential model. Inverted from the semi-variogram is the exponential covariogram model.

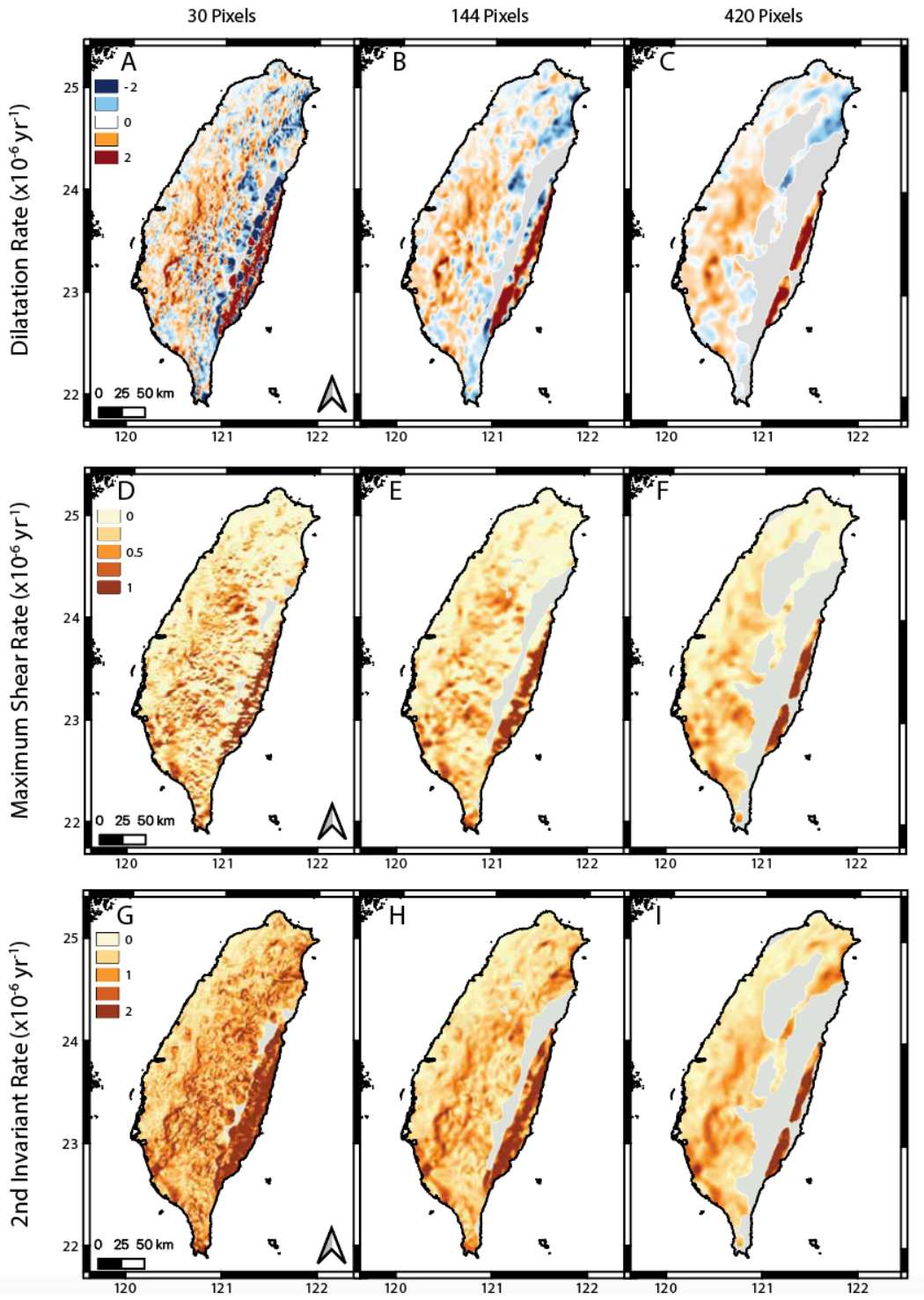

Figure S7. Deformation rate analysis with (A, B, C) dilatation rate, (D, E, F) maximum shear rate, and (G, H, I) 2nd invariant rate in (A, D, G) 30-pixel resolution, (B, E, H)144-pixel resolution, and (C, F, I) 420-pixel resolution. Positive dilatation values indicate contraction and negative values indicate expansion. High maximum shear values indicate increased shearing. 2nd invariant values describe both dilatation and maximum shear as total strain rate accumulation. Gray indicates regions of no data.

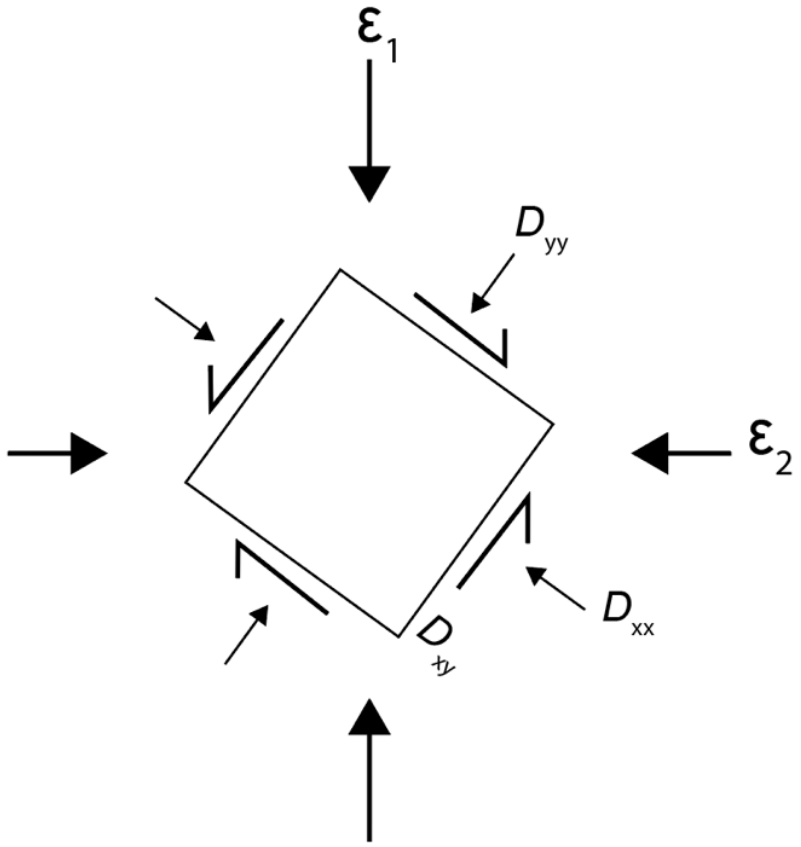

Figure S8. Schematic of maximum (ε_1) and minimum (ε_2) principal strains and the corresponding strain tensor components (D_{xx}, D_{yy}, D_{xy}) influencing a square. This schematic does not consider rotation.

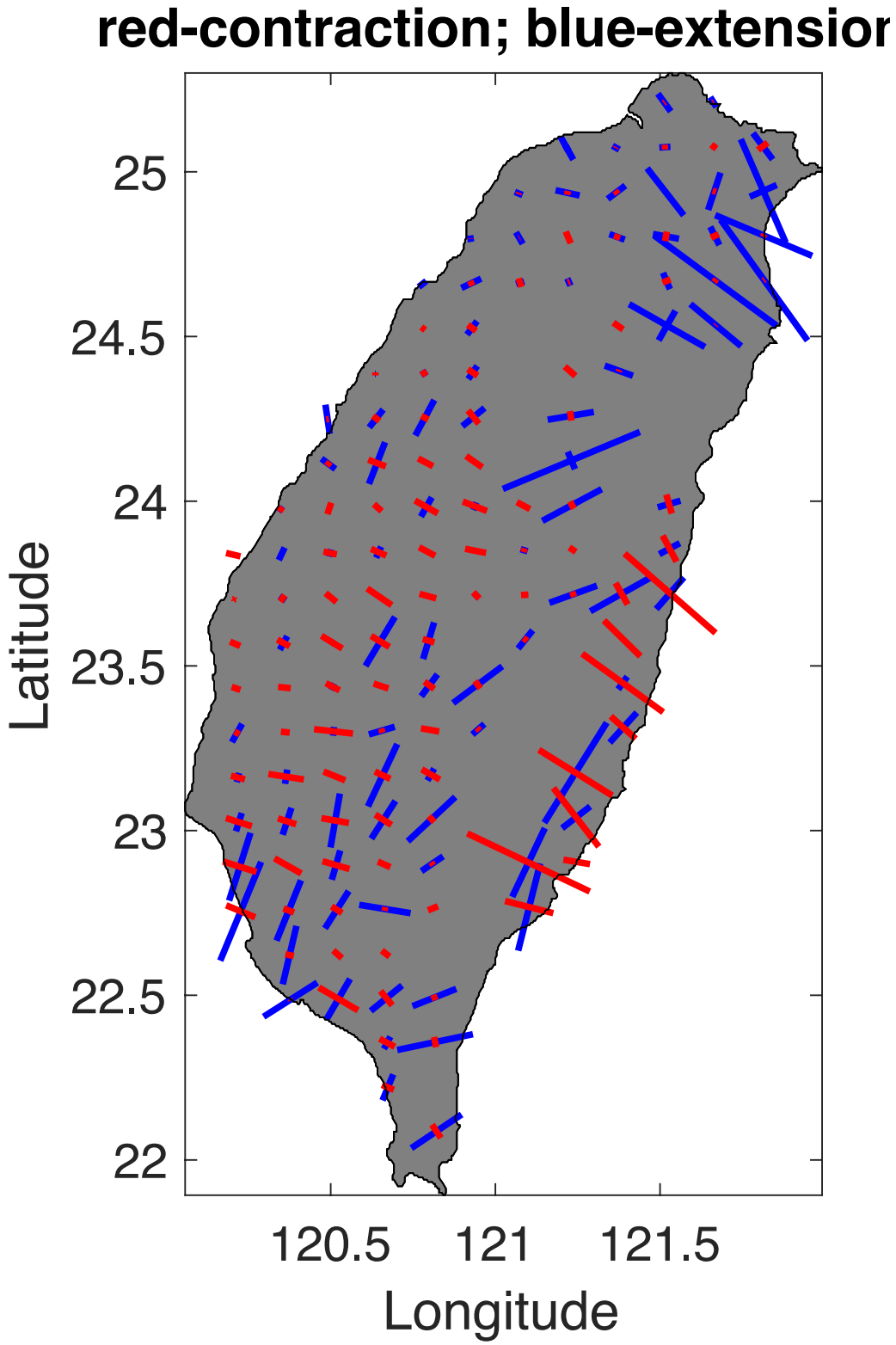

Figure S9. Overview of principal strain rates of Taiwan.

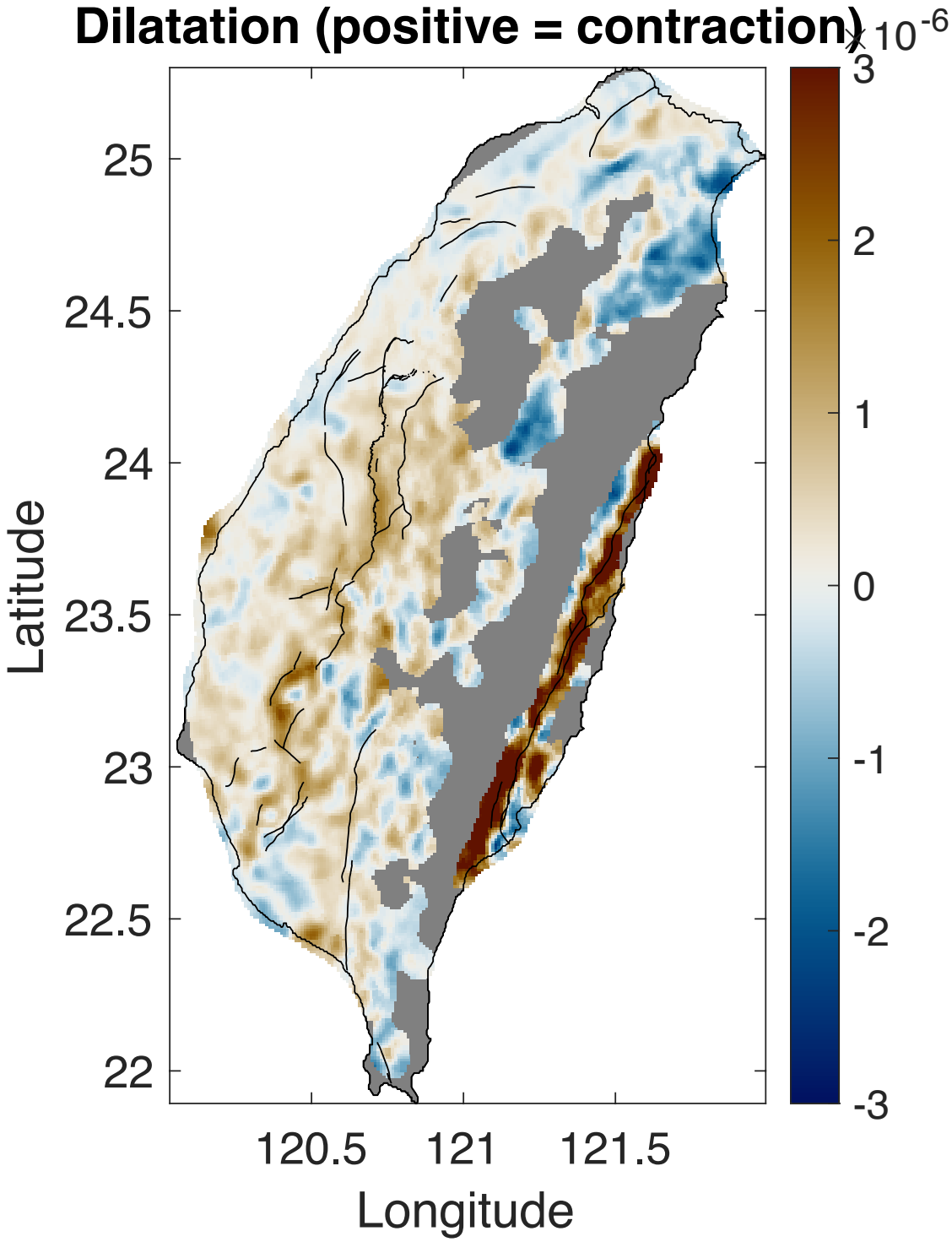

Figure S10. Overview of dilatation rate of Taiwan.

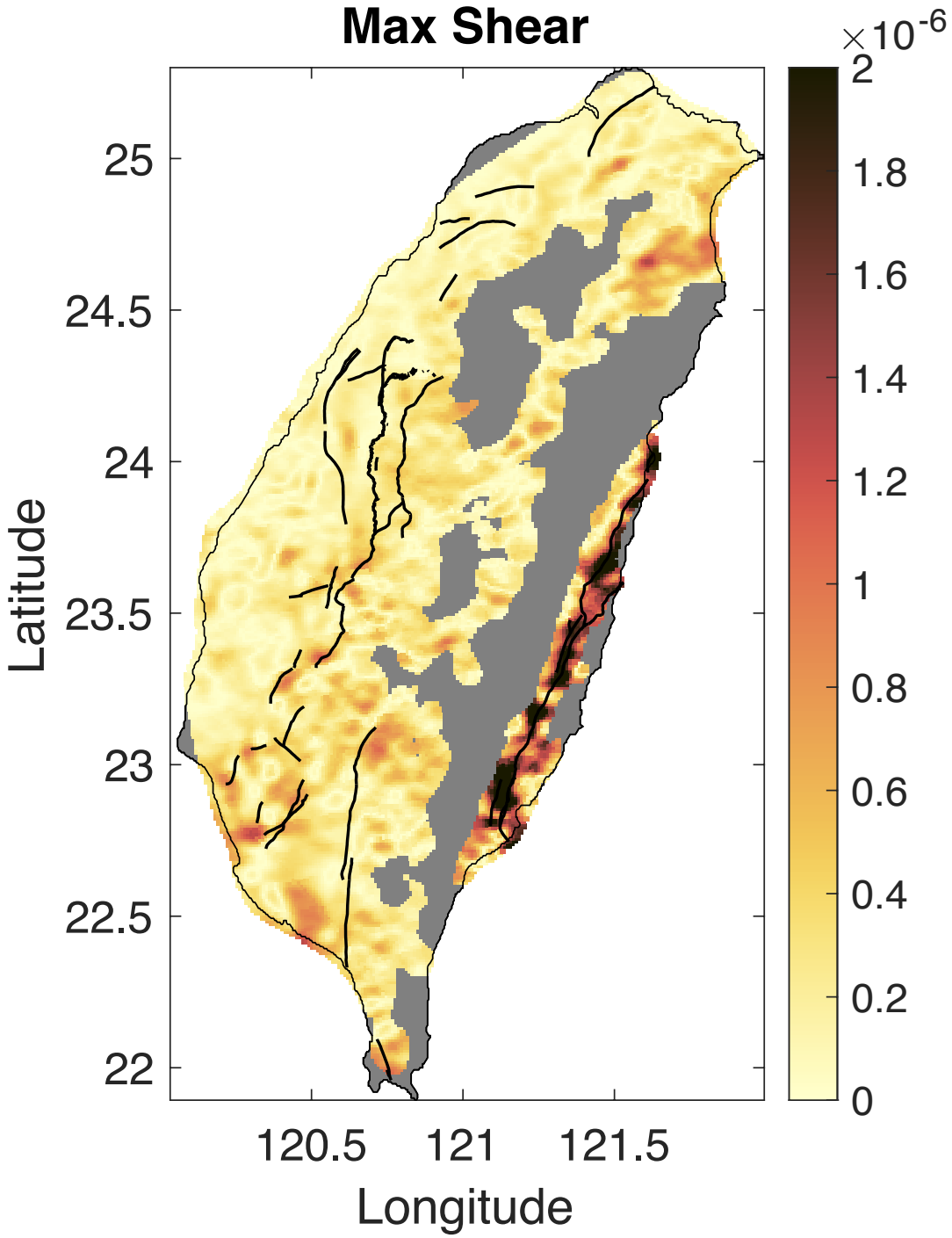

Figure S11. Overview of maximum shear rate of Taiwan.

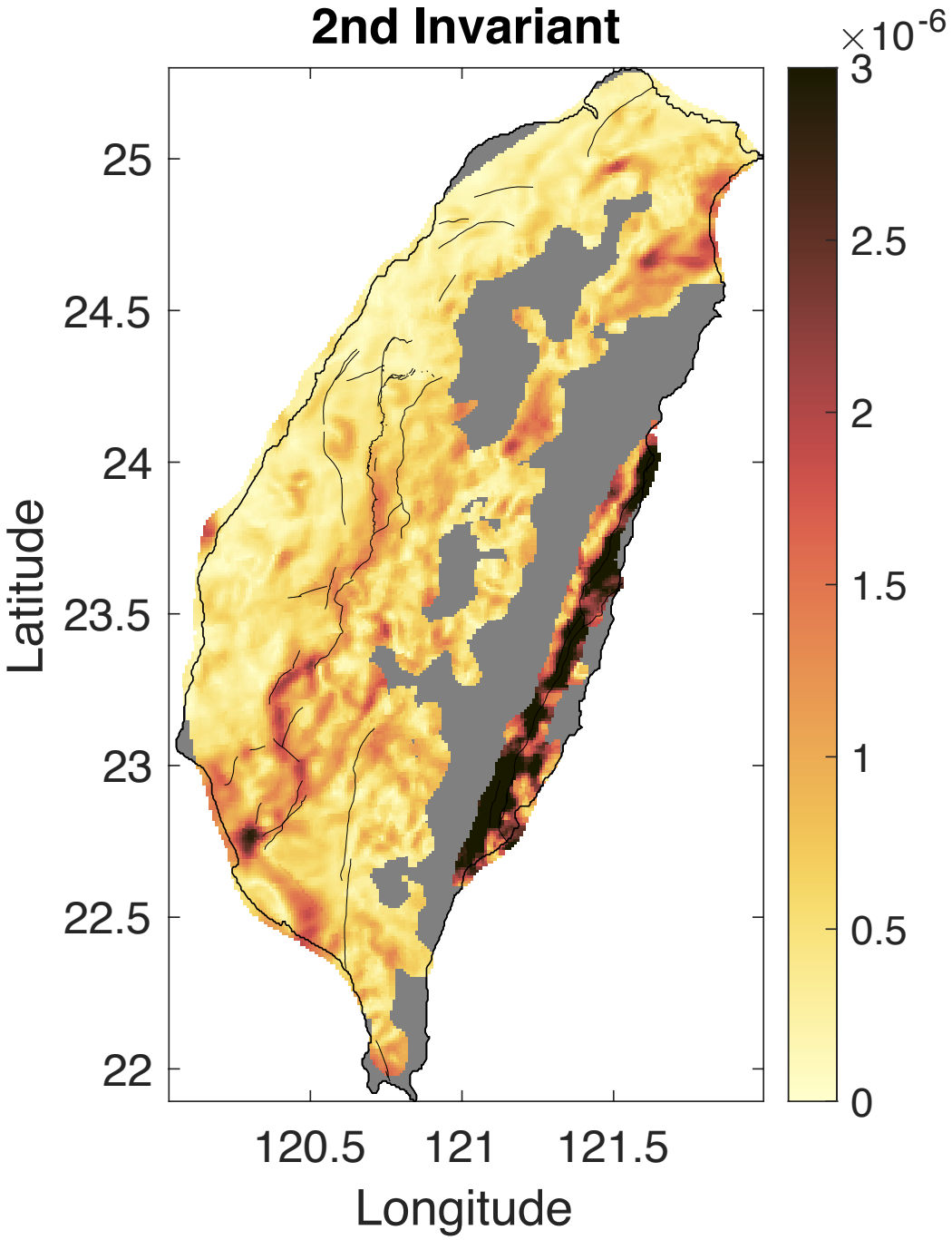

Figure S12. Overview of second invariant of the strain rate tensor of Taiwan.

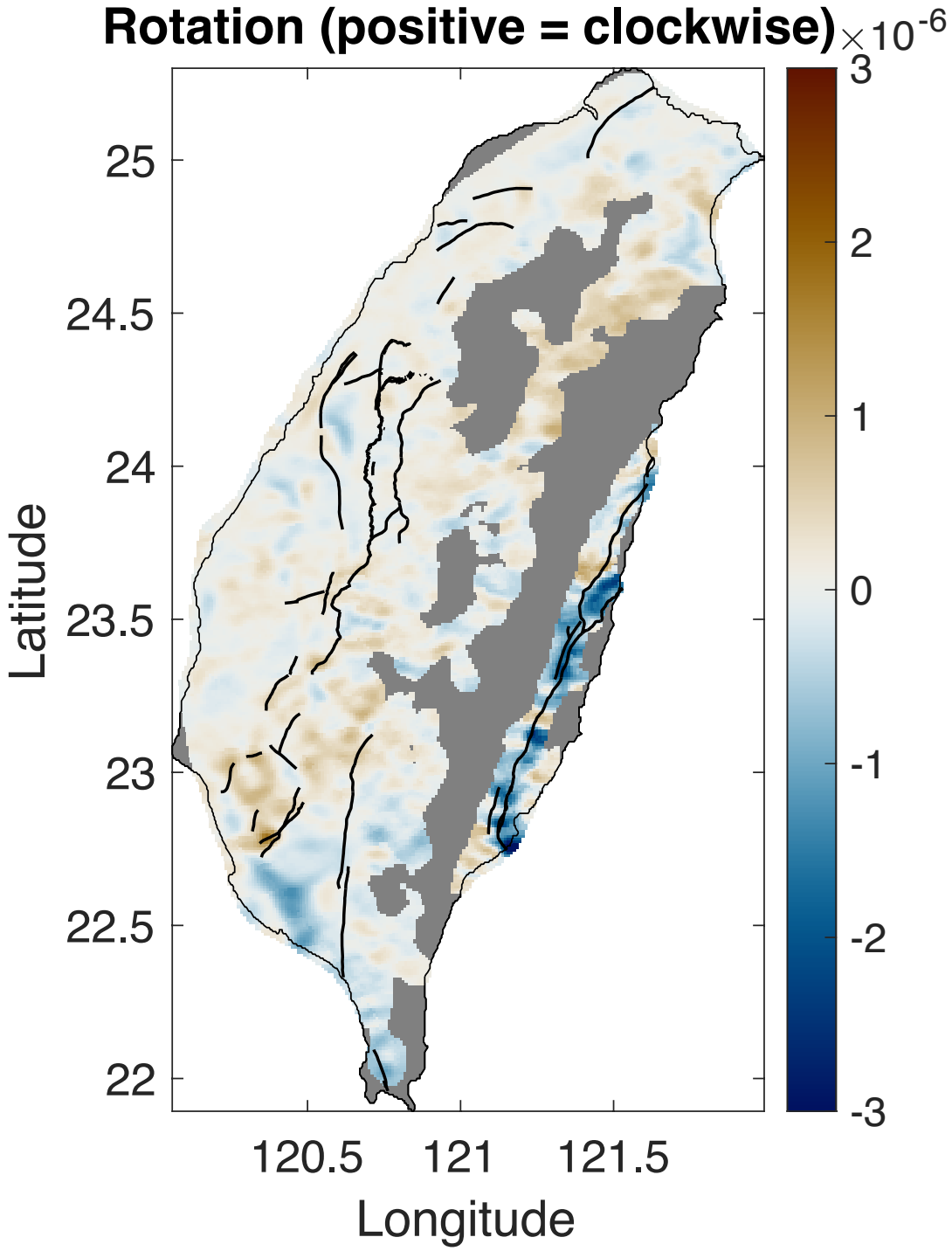

Figure S13. Overview of rotation rate of Taiwan.